Spatially uniform single-qubit gate operations with near-field microwaves and composite pulse compensation

C M Shappert[1,5]**, J T Merrill**[2]**, K R Brown**[1]**, J M Amini**[1]**, C Volin**[1]**,
S C Doret**[1]**, H Hayden**[1]**, C-S Pai**[1]**, K R Brown**[2,3,4] **and A W Harter**[1]

[1] Georgia Tech Research Institute, Atlanta, GA 30332, USA
[2] School of Chemistry and Biochemistry, Georgia Institute of Technology, Atlanta, GA 30332, USA
[3] School of Physics, Georgia Institute of Technology, Atlanta, GA 30332, USA
[4] School of Computational Science and Engineering, Georgia Institute of Technology, Atlanta, GA 30332, USA
E-mail: chris.shappert@gtri.gatech.edu

Abstract. We present a microfabricated surface-electrode ion trap with a pair of integrated waveguides that generate a standing microwave field resonant with the $^{171}\text{Yb}^+$ hyperfine qubit. The waveguides are engineered to position the wave antinode near the center of the trap, resulting in maximum field amplitude and uniformity along the trap axis. By calibrating the relative amplitudes and phases of the waveguide currents, we can control the polarization of the microwave field to reduce off-resonant coupling to undesired Zeeman sublevels. We demonstrate single-qubit π-rotations as fast as $1\,\mu s$ with less than 6% variation in Rabi frequency over an $800\,\mu m$ microwave interaction region. Fully compensating pulse sequences further improve the uniformity of X-gates across this interaction region.

[5] Author to whom any correspondence should be addressed.

IOP Institute of Physics   Φ DEUTSCHE PHYSIKALISCHE GESELLSCHAFT

Contents

1. Introduction

The future development of a fault-tolerant quantum processor will require the storage and manipulation of large numbers of qubits and the ability to execute quantum gates with high fidelity [1]. Some proposed architectures use trapped atomic ions to store and transport quantum information, and recent years have witnessed significant progress in the control of these systems [2–6]. Most trapped-ion experiments utilize laser fields to control internal and motional quantum states [7]; however, the fidelity of laser-mediated gates suffers from errors induced by unavoidable spontaneous emission [8–10], pointing instabilities and variations in the laser frequency, phase and power [11]. The systems required for laser-mediated gates are also large and complex, making them difficult to scale to the large numbers of qubits required to execute algorithms or simulations of interest.

Alternatively, microwaves can be used to control the ground electronic hyperfine state of the ions, and several experiments have demonstrated high-fidelity single-qubit gates that take advantage of the long natural lifetime of hyperfine qubits and the stability of microwave sources [12–15]. The advent of microfabricated ion traps allows microwave structures to be integrated directly into the trap, thereby facilitating strong fields and consequently fast gate operations. Many quantum algorithms require the parallel application of spatially uniform single qubit gates across groups of neighboring ions. Examples of such operations include the parallel application of gates across sub-regions of a surface code architecture [16] and the initialization of qubits into a computational basis. Global single qubit operations can also be used to apply dynamical decoupling techniques across all qubits to suppress dephasing errors [17]. In addition, small integrated microwave structures can enable single ion addressing and multi-qubit gate operations by generating strong field gradients [13, 14, 18–22].

Here we present a microfabricated surface electrode ion trap with integrated microwave waveguides that can apply global single qubit operations applicable to qubit initialization and dynamical decoupling. This trap was fabricated with standard very large-scale integration techniques. The waveguides are designed to place an antinode of a 12.64 GHz standing microwave field, suitable for coupling the ground state hyperfine levels of ^{171}Yb$^+$, at the center of the ion trap. The microwaves are polarization tunable, so that we can optimize coupling to a desired Zeeman transition while suppressing off-resonant coupling to neighboring transitions.
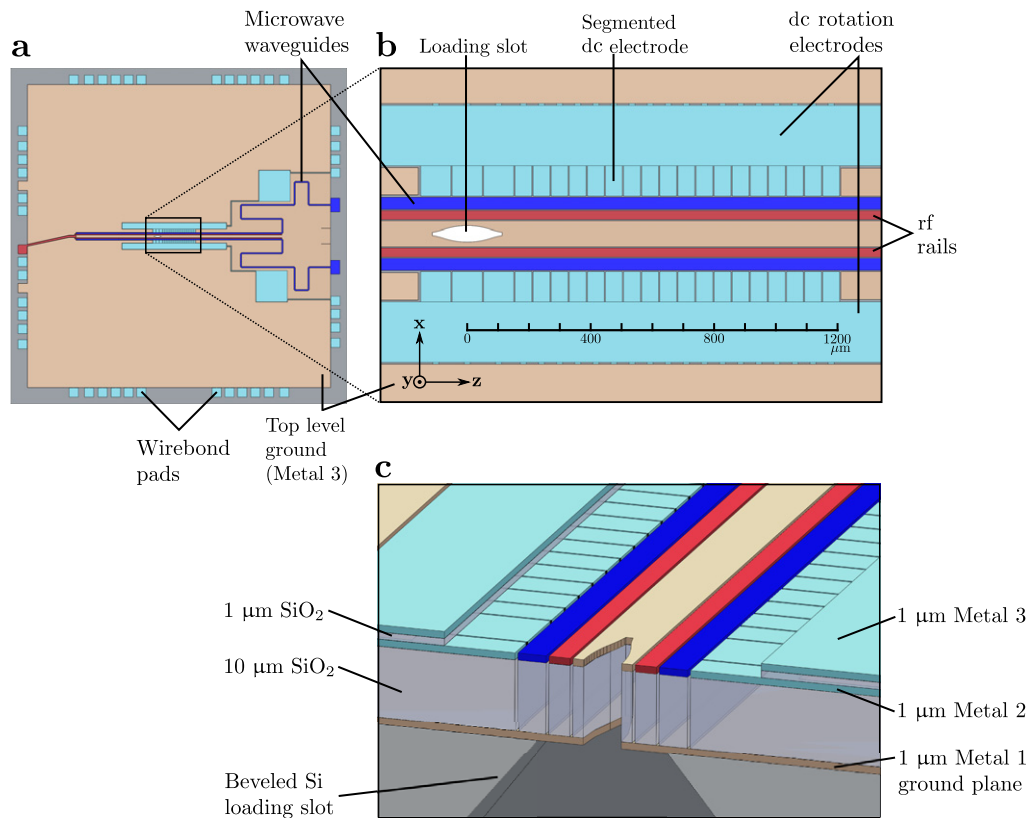
Figure 1. (a) A schematic view of the $11 \times 11 \, mm^2$ silicon chip. (b) The active trapping region, showing radio-frequency (rf) and dc trapping electrodes, the shaped loading slot and the on-chip microwave waveguides. (c) A cross section showing internal layers (the vertical direction is scaled by $10\times$ for visual clarity).

With the ion located $59 \, \mu m$ above the trap surface, a $0.037 \, mT$ field amplitude allows execution of sub-microsecond π-rotations. The intrinsic position dependence of the standing microwave field causes the Rabi frequency to vary by less than 6% over an $800 \, \mu m$ linear span. We correct for this residual non-uniformity by executing gates with fully compensating broadband pulse sequences.

2. Trap design

2.1. Trapping structures

The trap conforms to a symmetric five-wire surface-electrode Paul trap geometry [23] fabricated on a $11 \times 11 \, mm^2$ silicon die (figure 1(a)) similar to the designs reported in [24–26]. Electrodes etched into three sputtered aluminum layers are separated by insulating silicon dioxide films. rf potentials applied to two parallel electrodes provide radial ion confinement (in the x–y plane, figure 1(b)) $59 \, \mu m$ above the Metal 2 layer (figure 1(c)). Quasi-static potentials applied to segmented dc electrodes confine and transport ions along z. The rf electrodes are $30 \, \mu m$ wide along x with an inner edge-to-edge separation of $92 \, \mu m$. The segmented dc electrodes

are 56 μm wide along z except for six 100 μm wide electrodes bordering the loading slot. Two additional dc electrodes traversing the entire length of the trapping region are used to apply uniform x–y fields and to rotate the radial principal axes. Each electrode is separated from neighboring conductors by 4 μm gaps. Each dc electrode incorporates a 60 pF plate capacitor (1 mm^2 area) to filter unwanted rf pickup [24]. A loading slot allows a thermal beam of neutral Yb to reach the trapping volume from an oven located below the trap.

2.2. Integrated waveguides

The trap includes a pair of conductor-backed coplanar waveguides that generate local microwave magnetic fields. Each waveguide includes a 40 μm wide electrode with 4 μm gaps to neighboring conductors, and 10 μm of SiO$_2$ separate the coplanar layer from the ground plane below (figure 1(b)). The waveguides support a $\omega_{mw} = 2\pi \times 12.64$ GHz quasi-transverse electromagnetic (TEM) guided mode resonant with the hyperfine splitting between the $F = 0$ and 1 manifolds in the $^2S_{1/2}$ ground state of ^{171}Yb$^+$ (see figure 3(a)). In the ideal case, currents in each waveguide generate a magnetic field along the trapping axis

$$\vec{B}_k(z, t) = (\hat{x}\beta_{x,k} + \hat{y}\beta_{y,k}) I_k(z) \cos(\omega_{mw}t + \phi_k), \tag{1}$$

where $k = 1, 2$ is an index for the two waveguides, ϕ_k is the phase of the microwave current source, $I_k(z)$ is the current in each waveguide, and $\beta_{x,1} = \beta_{x,2} \simeq 0.08$ mT A^{-1} and $\beta_{y,1} = -\beta_{y,2} \simeq 0.17$ mT A^{-1} are properties of the waveguide mode. $\beta_{y,1} = -\beta_{y,2}$ due to the symmetric placement of the waveguides around the trapping axis. The waveguides terminate in an open circuit at a position that is approximately a quarter-wavelength from the trap center, which produces a standing wave field with maximum amplitude and uniformity in the gate region. A smaller traveling wave component also exists due to on-chip attenuation that generates an amplitude difference between forward and backward propagating waves. Although a traveling wave would produce more uniform fields, a standing wave produces a larger maximum field amplitude for a given input power. A standing wave design simplifies the trap by eliminating the need for on-chip resistive termination or for coupling power off the chip.

Far from the trap center, the waveguides meander to fit a complete wavelength on the chip and then terminate on wirebond pads at the edge of the chip. Extending the waveguides to a full wavelength in this way places a current node at the wirebond pads and reduces the potential for resistive power loss in the connections. A series of 25.4 μm diameter aluminum wirebonds connect the chip waveguides to two printed circuit board (PCB) waveguides that route microwaves from the edge of the trap package (figure 2). Connections between the PCB top level ground and the on-chip metal 1 and 2 ground planes are symmetric about each microwave electrode. Quarter-wave transformers match the 50 Ω impedance of the PCB waveguide to the 27 Ω on-chip characteristic impedance. The PCB is fabricated using a 254 μm thick Rogers 4350B substrate with two 18 μm thick copper foil conductive layers and a 3–6 μm electroless nickel immersion gold (ENIG) finish. The skin depth in the PCB at ω_{mw} is comparable to the thickness of the lossy nickel layer resulting in $\approx$3 dB of power loss between the microwave connector and wirebonds. Much of this power loss could be recovered by replacing the ENIG finish with an electroplated gold surface.
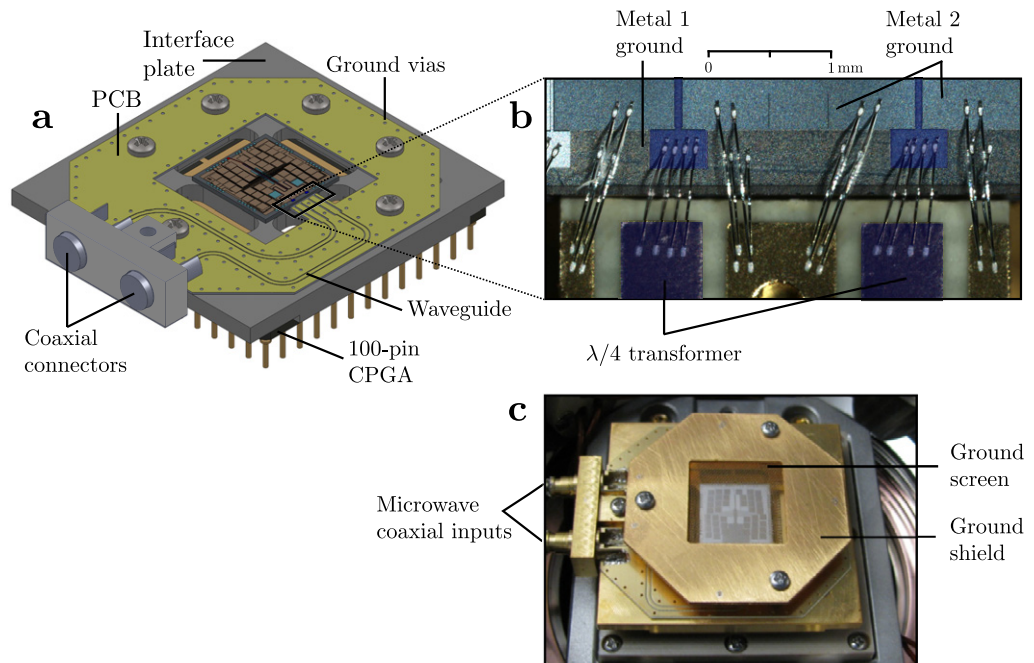
Figure 2. Components for trap packaging and microwave power delivery. (a) Schematic of a packaged trap with top ground screen removed for clarity. (b) Colorized photograph of the wirebond interface between the PCB and the trap die. (c) Photo of the installed device with coaxial microwave connections.

3. Trap performance

3.1. Microwave control of $^{171}Yb^+$ hyperfine qubits

Figure 3(a) shows the transitions in the ground state hyperfine manifold of $^{171}Yb^+$ addressed by the microwave field. A static 0.74 mT field along y defines the quantization axis and lifts the degeneracy of the $F = 1$ triplet. We select the clock states $|^2S_{1/2}, F = 1, m_F = 0\rangle \equiv |\uparrow\rangle$ and $|^2S_{1/2}, F = 0, m_F = 0\rangle \equiv |\downarrow\rangle$ as the qubit states. We observe Rabi oscillations at a frequency $\Omega = 2\pi \times 0.49$ MHz (figure 3(b)) by optically pumping into $|\downarrow\rangle$, applying microwave power for a variable interval of time, and measuring the resulting population transfer into the $F = 1$ manifold through state-selective fluorescence of the 369.5 nm cycling transition (figure 3(a)) [27].

Currents in each waveguide generate an oscillating magnetic field which contains both a π−polarized component that couples to the $\Delta m_F = 0$ clock transition and also a transverse-polarized component that couples to the $\Delta m_F = \pm 1$ transitions. Figure 3(c) shows the hyperfine spectrum measured with microwave power applied to a single waveguide. From the relative Rabi frequencies of the transitions, we estimate the ratio of polarization components for each waveguide as $|\beta_{x,k}|/|\beta_{y,k}| \approx 0.46$.

The polarization of the near-field microwaves may be controlled by adjusting the relative amplitude and phase of the microwave currents in the two waveguides. In particular, the polarization may be aligned along the quantization axis, thereby maximizing the qubit transition
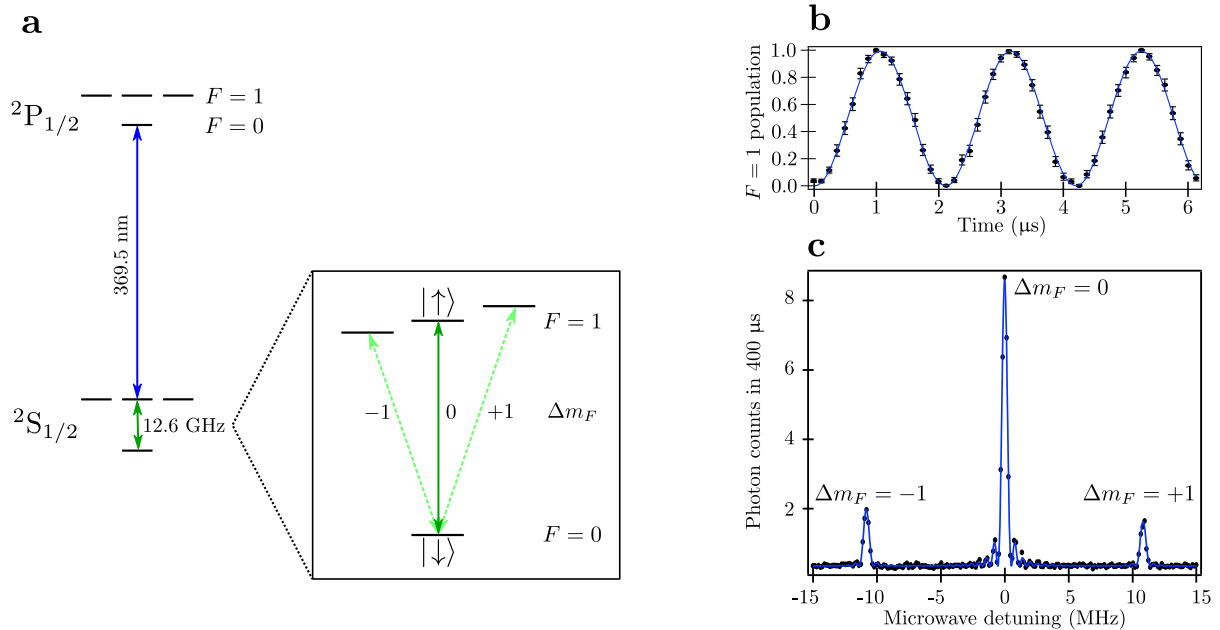
Figure 3. (a) Simplified energy level structure of the ^{171}Yb$^+$ ion (not to scale). The qubit uses the $|F = 1, m_F = 0\rangle \equiv |\uparrow\rangle$ and $|F = 0, m_F = 0\rangle \equiv |\downarrow\rangle$ clock states. During experiments, a 12.64 GHz microwave field produced by on-chip waveguides couples hyperfine states in the $^2S_{1/2}$ manifold. The $^2S_{1/2} \rightarrow ^2P_{1/2}$ transition at 369.5 nm is used for Doppler-cooling, qubit initialization, and qubit detection [27]. (b) Rabi oscillations between the qubit states induced by application of microwaves ($z = 300\,\mu$m). (c) Resolved hyperfine transitions between $^2S_{1/2}$ sublevels.

Rabi frequency while also suppressing off-resonant $\Delta m_F = \pm 1$ transitions. The active and passive microwave components supplying energy to these electrodes are not perfectly power-balanced and phase-matched. We calibrate the microwave sources by first driving each waveguide independently to map the relationship between source power and Rabi frequency (figure 4(a)). Once the field amplitudes from the waveguides have been equalized, the relative phase between microwave currents ϕ_r can be varied to produce an arbitrary linear polarization in the $x-y$ plane. Figure 4(b) shows the resonant Rabi frequency for each of the three transitions as ϕ_r is varied, demonstrating the desired suppression of the $\Delta m_F = \pm 1$ transitions at $\phi_r = \pi$. The minimum measured Rabi frequencies of the $\Delta m_F = \pm 1$ transitions are less than 8% of the $\Delta m_F = 0$ frequency. We suspect that the suppression is limited by a residual z component of the quantization field, and the mismatch between the $\Delta m_F = \pm 1$ curves in figure 4(b) is caused by frequency dependence in the microwave delivery system.

Polarization control is useful with any hyperfine qubit because it can suppress unwanted transitions as gate speeds are increased or Zeeman splittings are reduced. In the context of the experiments presented here, with a 10.4 MHz Zeeman splitting and $\Omega = 2\pi \times 0.5$ MHz, off-resonant coupling would limit the fidelity of a $\pi/2$ gate (square envelope) to $\mathcal{F} < 1 - 4 \times 10^{-4}$ if only a single microwave waveguide were used.
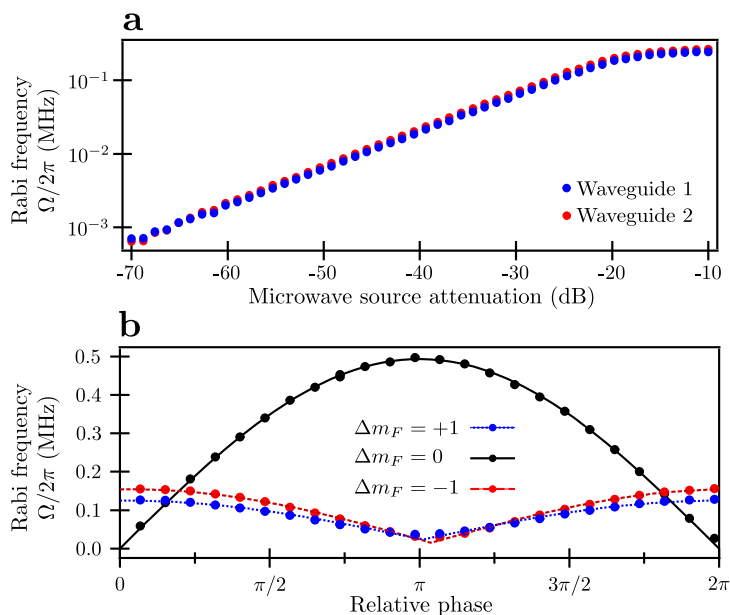
Figure 4. (a) Plot of the qubit Rabi frequency versus microwave source attenuation, obtained with a resonant field produced by a single waveguide. The nonlinearity at high source power is caused by amplifier saturation. (b) Polarization control via microwave power balancing and phase tuning between the two waveguides. The solid curves are fits to the magnitude of a sinusoid.
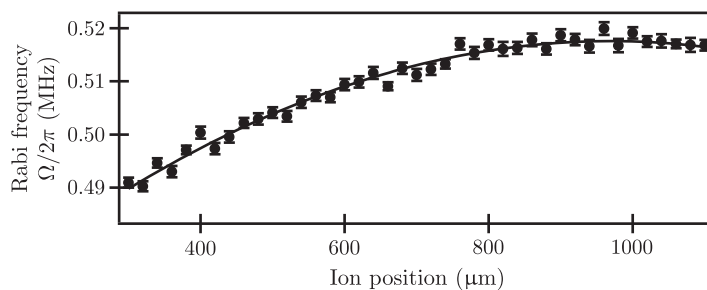

Figure 5. Measured Rabi frequency of the qubit transition as a function of the axial distance from the load slot center. The solid line is a quadratic fit to the data which indicates a maximum microwave field at $z = 957 \, \mu$m.

3.2. Microwave field uniformity and compensation

The standing wave current in the waveguides produces a microwave field with non-uniform amplitude along the trap axis. Figure 5 shows the measured Rabi frequency of the qubit transition at several positions along the trap axis. We observe a maximum Rabi frequency of $2\pi \times 0.52$ MHz, corresponding to a field amplitude of 0.037 mT, located $z_0 = 957 \, \mu$m from the loading slot center. Finite element calculations predict an antinode location at $z = 895 \, \mu$m in reasonable agreement with the experiment. These models indicate that the maximum field corresponds to a local current in each electrode of $I_z(z_0) \approx 0.1$ A. The maximum Rabi frequency
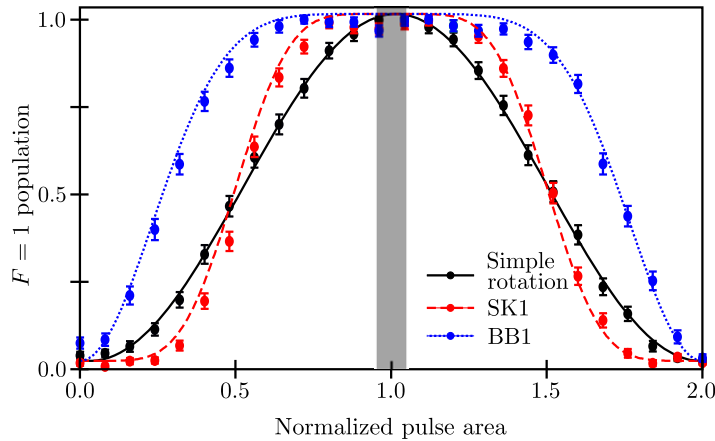
Figure 6. Population transfer into the $F = 1$ manifold after applying a logical X-gate produced by simple pulses (black), SK1 (red), and BB1 (blue) sequences. The pulse areas are uniformly scaled by adjusting the pulse lengths. The curves are the signals predicted by theory, adjusted to account for a known qubit-detection error. The shaded area encloses the range of systematic microwave amplitude error observed over the entire trapping region.

is presently limited by the output power of the 3 W amplifiers and losses in the microwave delivery system (see the appendix). Heating due to on-chip dissipation in the 1 μm thick aluminum electrodes would ultimately determine the maximum current density and associated Rabi frequency.

The microwave field non-uniformity appears as an effective amplitude error when implementing global single-qubit rotations on multiple ions located at different positions in the trap. To improve single-qubit gate uniformity, we implement global gates using broadband compensating pulse sequences [28, 29]. This technique replaces a simple pulse with a sequence of pulses whose phases are chosen to nearly cancel the effective microwave amplitude error. The excitation profiles of such pulse sequences enable global rotations on many qubits, although the microwave amplitude may differ significantly between distant ions.

Here we demonstrate the error-canceling properties of composite X-gates constructed from the first-order SK1 [30, 31] and second-order BB1 [32] sequences. The experiments prepare the qubit in $|\downarrow\rangle$, apply a logical X-gate, and then measure the population in the $F = 1$ manifold. To simulate the effect of systematic over/under rotations, we uniformly scale the pulse areas of every pulse in the sequence by adjusting the pulse duration. Figure 6 plots the measured excitation profiles produced by compensated gates, overlayed on the signal predicted by theory. Gates performed with the BB1 sequence are more robust to large variations in pulse area and require no additional time to execute compared to SK1, therefore BB1 is a superior choice for compensating the non-uniform field amplitude observed in figure 5. In contrast, the passband behavior of the SK1 sequence may make it a better choice for applications where localized gates are a primary objective. Assuming the field non-uniformity is the sole source of error, we calculate theoretical fidelities of X-gates. For the 6% amplitude deviation observed at $z = 300 \, \mu$m, a simple rotation performs a global X-gate with a minimum fidelity $\mathcal{F} \geqslant 0.995$, whereas SK1 and BB1 perform the same gate with minimum fidelities of $\mathcal{F} \geqslant 1 - 1.5 \times 10^{-4}$ and $1 - 2.2 \times 10^{-7}$, respectively.
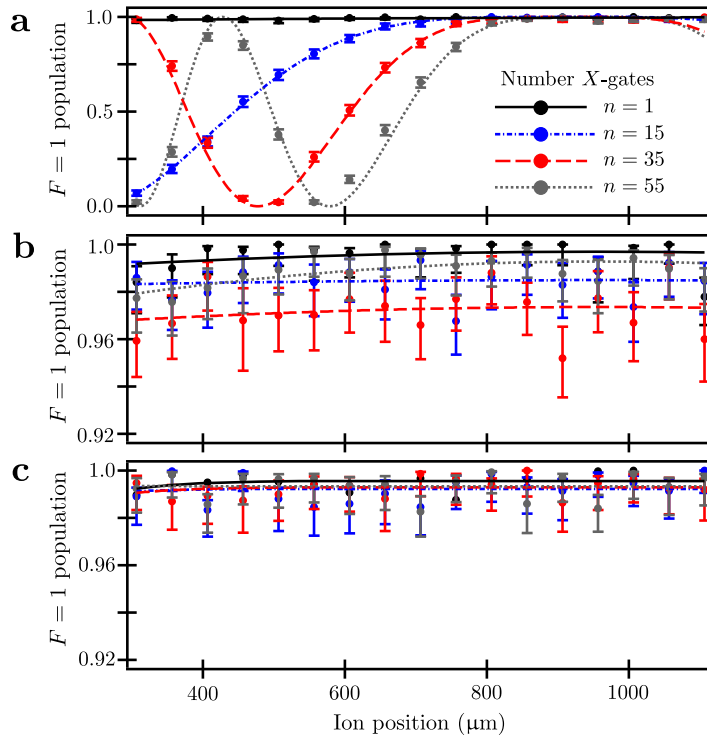
Figure 7. Excited state population fraction after application of n sequential Pauli X-gates, with each gate implemented via (a) a simple rotation operator with no compensating pulse sequence, (b) SK1 composite pulse sequence or (c) BB1 composite pulse sequence. Lines are fits to curves predicted by theory given the position-dependent Rabi frequency shown in figure 5.

As a demonstration of uniform global gates, we perform an experiment where n sequential logical X-gates are applied to a qubit initialized in $|\downarrow\rangle$. We calibrate gate times so that an ion located at the microwave amplitude maximum ($z_0 = 957\,\mu$m) experiences nearly perfect rotations. Qubits displaced from the field maximum rotate at lower Rabi frequencies, acquiring an under-rotation error that accumulates as n increases. We measure the $F = 1$ population as a function of ion axial position and number of sequential X-gates. For X-gates implemented by simple rotations we observe fringes (figure 7(a)) arising from the local qubit falling behind by an entire Rabi cycle relative to the maximal Rabi frequency. Instead, when implementing SK1 or BB1 pulses (figures 7(b) and (c)) the error accumulates so slowly that the excitation profile remains flat over the trapping region after $n = 55$ logical X-gates. Our ability to resolve fringe structure in these cases is currently limited by systematic state-preparation and measurement errors and by the number of simple pulse operations we can implement. In theory, neither the BB1 nor the SK1 sequence imposes a penalty on the maxiumum achievable fidelity when the primary sources of error can be compensated by the sequences, and we observe no reduction in $F = 1$ population due to the pulse sequences at the field calibration position, z_0, within our measurement error.

We analytically calculate the fidelity scaling of the sequential logical X-gates as a function of the microwave field strength. For simple rotations, the fidelity drops as $\mathcal{F} = |\cos[\epsilon(z)\pi n/2]|$, where $\epsilon(z) = [\Omega(z) - \Omega(z_0)]/\Omega(z_0)$ is the fractional difference in Rabi frequencies between

the ion location z and the field maximum. For SK1 pulses the fidelity scales as $\mathcal{F} = |1 - \frac{15}{128}\pi^4\epsilon(z)^4 n + O(\epsilon(z)^6)|$, and for BB1 the fidelity scales as $\mathcal{F} = |1 - \frac{5}{1024}\pi^6\epsilon(z)^6 n + O(\epsilon(z)^8)|$.

4. Conclusion

We developed a microfabricated surface-electrode ion trap with integrated microwave waveguides that performs arbitrary single-qubit gates on the $^{171}\mathrm{Yb}^+$ hyperfine qubit. The polarization of the local microwave field can be tuned to minimize off-resonant coupling to adjacent Zeeman sub-levels. This suppression of off-resonant coupling will be most useful when Rabi frequencies are large compared to the Zeeman splittings, thus causing reduced spectral resolution of neighboring transitions. We demonstrate the use of fully compensating pulse sequences to reduce single-qubit gate variation caused by a spatially non-uniform microwave amplitude. Similar passband and narrowband pulse sequences [29] could be used to exploit microwave amplitude variations to enable single-ion addressing without requiring perfect field suppression at the location of neighboring ions.

Acknowledgments

Appendix. Methods

A.1. Microwave delivery system

A schematic view of the microwave supply system is shown in figure A.1. An Agilent 83623B Swept-Signal Generator provides a stable microwave local oscillator (LO) signal that is approximately 300 MHz detuned from the qubit resonant frequency near 12.64 GHz. Delivery of this signal is controlled by an American Microwave SW-218 high-speed rf switch. The signal is split to supply the local oscillator ports of two frequency mixers. Two separate direct digital synthesis (DDS) boards with synchronized clocks supply the intermediate frequency (IF) signals near 300 MHz. The DDS outputs have independently controllable amplitude, phase and frequency and these signals are amplified prior to mixing with the LO signal. The mixers reject the carrier frequency and produce two rf sidebands at $\omega_{\mathrm{mw}} = \omega_{\mathrm{lo}} \pm \omega_{\mathrm{dds}}$ where one of these sidebands is tuned to the frequency of the desired hyperfine transition, while the other is far off resonance. Both signals are amplified in separate Mini-Circuits ZVE-3W-183+ amplifiers and routed to a coaxial feedthrough port on the UHV chamber. A pair of circulators protect the amplifiers from accidental high power reflections and also provide a dc ground on the microwave lines. Inside the chamber the microwaves are carried by two coaxial lines with Kapton dielectric and braided conductor, selected for UHV compatibility. The combined power loss in the feedthrough and Kapton cables is $\approx 5.3\,\mathrm{dB}$.
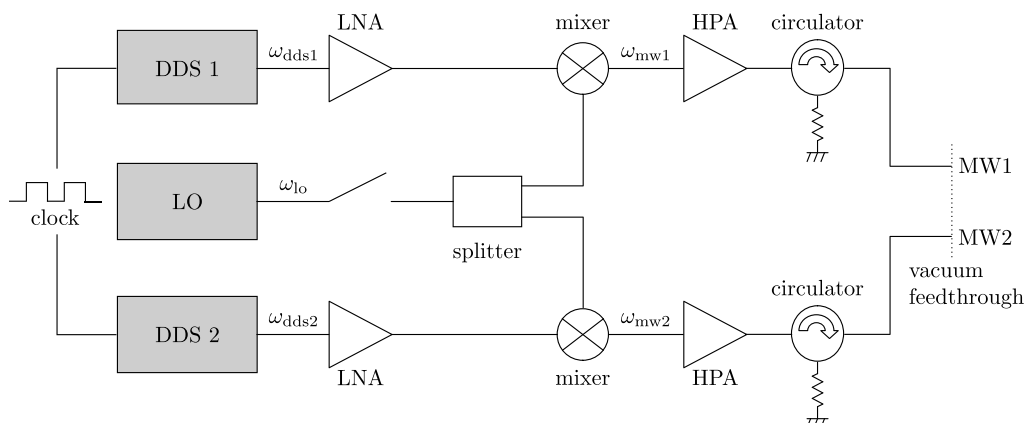
Figure A.1. Schematic view of microwave delivery system connected to the outside of the UHV chamber. The two DDS sources are mixed with a stable local oscillator and provide independent control over the amplitude, phase, and frequency ($\omega_{mw} = \omega_{lo} \pm \omega_{dds}$) of the microwave signal applied to the trap waveguides, though during typical operation $\omega_{dds1} = \omega_{dds2}$. DDS—direct digital synthesizer, LO—local oscillator, LNA—low noise amplifier, HPA—high power amplifier, MW—microwave.

A.2. Trap packaging

We mount chips to a gold electroplated stainless steel plate that also serves as a structurally rigid platform for mounting other components, including microwave connectors, PCB, grounded screen and a 100-pin ceramic pin-grid array (CPGA). Vacuum compatible Au/Sn solder bonds the microwave connectors (Corning Gilbert GPO) to the top metal layer of the PCB, and a retention block secures these connectors to the steel plate to reduce stress in the solder joints. The chip is bonded to the interface plate with electrically conductive epoxy (Epoxy Technology H21D) which accommodates the differential thermal expansion between the stainless steel mounting plate and the silicon chip during vacuum bake-out. Wire bonds at the chip perimeter establish electrical connections to the CPGA to provide both dc and rf trapping potentials, while wire bonds to the PCB supply microwave energy to the chip (figure 2(b)). To minimize scattered laser light, wire bonds are excluded from regions where cross-chip laser access is required.

References

[1] DiVincenzo D P 2000 The physical implementation of quantum computation *Fortschr. Phys.* **48** 771–83
[2] Wineland D and Leibfried D 2011 Quantum information processing and metrology with trapped ions *Laser Phys. Lett.* **8** 175–88
[3] Monroe C and Duan L M 2010 Quantum networks with trapped ions *Rev. Mod. Phys.* **82** 1209–24
[4] Häffner H *et al* 2008 Quantum computing with trapped ions *Phys. Rep.* **469** 155–203
[5] Benhelm J *et al* 2008 Towards fault-tolerant quantum computing with trapped ions *Nature Phys.* **4** 463–6
[6] Home J *et al* 2009 Complete methods set for scalable ion trap quantum information processing *Science* **325** 1227–30
[7] Leibfried D *et al* 2003 Quantum dynamics of single trapped ions *Rev. Mod. Phys.* **75** 281–324

[8] Ozeri R *et al* 2005 Hyperfine coherence in the presence of spontaneous photon scattering *Phys. Rev. Lett.* **95** 030403

[9] Ozeri R *et al* 2007 Errors in trapped-ion quantum gates due to spontaneous photon scattering *Phys. Rev. A* **75** 042329

[10] Akerman N *et al* 2012 Reversal of photon-scattering errors in atomic qubits *Phys. Rev. Lett.* **109** 103601

[11] Wineland D J *et al* 1998 Experimental issues in coherent quantum-state manipulation of trapped atomic ions *J. Res. Natl Inst Stand. Technol.* **103** 259

[12] Brown K R *et al* 2011 Single-qubit-gate error below 10^{-4} in a trapped ion *Phys. Rev. A* **84** 030303

[13] Ospelkaus C *et al* 2011 Microwave quantum logic gates for trapped ions *Nature* **476** 181–4

[14] Allcock D *et al* 2013 A microfabricated ion trap with integrated microwave circuitry *Appl. Phys. Lett.* **102** 044103

[15] Timoney N *et al* 2011 Quantum gates and memory using microwave-dressed states *Nature* **476** 185–8

[16] Fowler A G *et al* 2012 Surface codes: towards practical large-scale quantum computation *Phys. Rev. A* **86** 032324

[17] Biercuk M J *et al* 2009 Optimized dynamical decoupling in a model quantum memory *Nature* **458** 996–1000

[18] Warring U *et al* 2013 Individual-ion addressing with microwave field gradients *Phys. Rev. Lett.* **110** 173002

[19] Warring U *et al* 2013 Techniques for microwave near-field quantum control of trapped ions *Phys. Rev. A* **87** 013437

[20] Johanning M *et al* 2009 Individual addressing of trapped ions and coupling of motional and spin states using rf radiation *Phys. Rev. Lett.* **102** 073004

[21] Ospelkaus C *et al* 2008 Trapped-ion quantum logic gates based on oscillating magnetic fields *Phys. Rev. Lett.* **101** 090502

[22] Wang S *et al* 2009 Individual addressing of ions using magnetic field gradients in a surface-electrode ion trap *Appl. Phys. Lett.* **94** 094103

[23] Chiaverini J *et al* 2005 Surface-electrode architecture for ion-trap quantum information processing *Quantum Inf. Comput.* **5** 419–39

[24] Doret S C *et al* 2012 Controlling trapping potentials and stray electric fields in a microfabricated ion trap through design and compensation *New J. Phys.* **14** 073012

[25] Merrill J T *et al* 2011 Demonstration of integrated microscale optics in surface-electrode ion traps *New J. Phys.* **13** 103005

[26] Wright K *et al* 2013 Reliable transport through a microfabricated X-junction surface-electrode ion trap *New J. Phys.* **15** 033004

[27] Olmschenk S *et al* 2007 Manipulation and detection of a trapped Yb$^+$ hyperfine qubit *Phys. Rev. A* **76** 052314

[28] Levitt M H 1986 Composite pulses *Prog. Nucl. Mag. Res. Spec.* **18** 61–122

[29] Merrill J T and Brown K R 2012 Progress in compensating pulse sequences for quantum computing arXiv:1203.6392v1

[30] Brown K R *et al* 2004 Arbitrarily accurate composite pulse sequences *Phys. Rev. A* **70** 052318

[31] Brown K R *et al* 2005 Erratum: arbitrarily accurate composite pulse sequences (*Phys. Rev. A* 70 052318 (2004)) *Phys. Rev. A* **72** 039905

[32] Wimperis S 1994 Broadband, narrowband, and passband composite pulses for use in advanced NMR experiments *J. Magn. Reson. A* **109** 221–31